Submitted to the 29th International Conference on High-Energy Physics ICHEP98,
Vancouver, Canada, July 1998

Measurement of Dijet Cross Sections in Deep-Inelastic Scattering at HERA and a Direct Determination of the Gluon Density in the Proton

H1 Collaboration

Abstract

Dijet cross sections in deep-inelastic scattering have been measured with the H1 detector at the positron proton collider HERA using data taken in the years 1994 – 1997 corresponding to an integrated luminosity of $\mathcal{L}_{int} \simeq 36$ pb^{-1}. A large kinematical range of squared four momentum transfers $10 < Q^2 < 5000$ GeV^2, squared transverse jet energies $70 < E^2_{\perp\text{Breit}} < 1200$ GeV^2 and invariant dijet masses $200 < M^2_{jj} < 7000\ \mathrm{GeV}^2$ is covered. For the first time in this kinematical region double differential dijet cross sections have been measured for several sets of variables with different $k_\perp$ cluster jet algorithms. The results are compared to perturbative QCD calculations in next-to-leading order in the strong coupling constant. Over the whole phase space the next-to-leading order predictions give a very good description of the data. In a NLO QCD fit to the dijet cross sections we have determined the gluon density in the proton for $0.01 < x < 0.1$ at a scale $\mu^2 = 200\,\mathrm{GeV}^2$. The result is in good agreement with the gluon density from a QCD analysis of H1 structure function data and extends the determination to larger x.

Abstract: 520
Parallel sessions: 3,5
Plenary sessions: 5,7

1 Introduction

The large center-of-mass energy ($\sqrt{s} \approx 300$ GeV) available at HERA colliding 27.5 GeV positrons on 820 GeV protons offers a large phase space for the hadronic final state in deep-inelastic scattering (DIS). This allows clean jet structures to be observed.

Perturbative QCD is expected to give a good description of hard processes. While for the inclusive DIS cross section the squared transverse momentum transfer, Q^2, is the hard scale, in dijet production the transverse jet energy $E_\perp$ is an additional hard scale. Hard processes can be investigated as a function of both of these scales and the predictions of perturbative QCD can be tested. Particularly suited for such quantitative studies is the Breit frame where the virtual photon collides head-on with the proton. In this frame the transverse jet energy[1] ($E_{\perp\mathrm{Breit}}$) directly reflects the hardness of the underlying QCD process.

High E_T jets emerge due to a large fraction from gluon initiated processes. Dijet production is therefore directly sensitive to the strong coupling constant α_s and the gluon density in the proton $G(x, Q^2)$. Since the start-up of HERA, the possibility to perform QCD precision test has stimulated a lot of theoretical and experimental activity. Meaningful quantitative predictions of perturbative QCD are only possible in next-to-leading order α_s (NLO). Since early NLO predictions [1, 2] were only available in the form of semi-analytical calculation restricted to the modified JADE algorithm [3, 4], experimental analyses were performed with this algorithm [5–8]. From a theoretical point of view, the JADE jet algorithm has however several disadvantages [9–11]. Meanwhile flexible NLO Monte Carlo programs [12–15] allow arbitrary jet definition schemes and experimental cuts. Quantitative agreement between data and NLO predictions could nevertheless only be achieved in restricted phase space regions. Especially in the domain of $Q^2 \lesssim 40\ \mathrm{GeV}^2$ the production rates of hard jets could not be understood by fixed order QCD calculations. Recently significant progress has been made how data can be compared to NLO calculations in a meaningful way. In an analysis of dijet rates defined by the cone algorithm [16] for the first time agreement between NLO calculations and data could be established [17] in the low Q^2 domain.

In this paper we present a comprehensive measurement of double differential dijet cross sections in the Breit frame corrected for detector effects from $10 < Q^2 < 5000\ \mathrm{GeV}^2$ covering $70 \lesssim E^2_{\perp\mathrm{Breit}} \lesssim 1200\ \mathrm{GeV}^2$ and invariant dijet masses of $200 \lesssim M^2_{jj} \lesssim 7000\ \mathrm{GeV}^2$. Several $k_\perp$ jet cluster algorithms are used in the analysis. We compare the data to the predictions of NLO calculations. Furthermore we perform a NLO QCD fit to these data and determine the gluon density in the proton at fractional proton momenta $0.01 < x < 0.1$ and a scale of $\mu_f^2 = 200\,\mathrm{GeV}^2$.

The paper is organized as follows: In section 2 we describe the QCD models used for the correction of the data and the NLO calculation to which the results are compared. In section 3 we introduce the jet algorithms used in the analysis and define the measured observables. Section 4 gives a brief description of the H1 detector. The data selection and the correction procedure are described in sections 5 and 6. The dijet cross sections are presented in section 7 and compared to NLO calculations. In section 8 the gluon density is determined.

[1] "transverse" refers to the z-axis which is given by the axis of the virtual photon and the proton.

2 Monte Carlo Models and NLO Calculations

A simulation of the detailed properties of the hadronic final state in deep-inelastic scattering events is available in form of Monte Carlo event generators. They usually include the matrix element of the hard subprocess in first order of the strong coupling constant α_s, QCD radiation effects and a model to describe the non-perturbative transition from partons to hadrons.

The LEPTO Monte Carlo [18] incorporates the $\mathcal{O}(\alpha_s)$ QCD matrix element and takes higher order parton emissions approximately into account using the concept of parton showers [19] based on the leading logarithm DGLAP equations [20]. QCD radiation can occur before and after the hard subprocess. The formation of hadrons is performed using the LUND string model [21] implemented in JETSET [22].

The HERWIG Monte Carlo [23] only differs in details from the above described QCD treatment and relies on leading logarithm parton showers with additional matrix element corrections [24]. It implements the cluster fragmentation model [25]. ARIADNE [26] treats the hard subprocess and the QCD shower evolution differently. Gluon emissions are treated by the colour dipole model [27] assuming a chain of independent radiating dipoles spanned by colour connected partons. The first emission in the cascade is corrected by the matrix element to first order α_s [28].

DJANGO [29] provides an interface between the event generator LEPTO or ARIADNE and HERACLES [30] which includes the full electroweak matrix element to calculate radiative corrections.

Calculations in next-to-leading order of the strong couling constant α_s (DISENT [13], MEPJET [12], DISASTER++ [14] and JETVIP [15]) have recently been made available in the form of flexible Monte Carlo generators. They allow any jet definition scheme and arbitrary phase space cuts to be applied on a three parton configuration. They do not include any fragmentation. These programs have been compared for several observables and, in general, a satisfactory agreement was found [14, 31, 32]. In this analysis DISENT is used. We have modifed the program such that the electromagnetic coupling constant changes as a function of Q^2.

3 Jet Definition and Observables

The dijet analysis is performed in the Breit frame (defined by $\vec{q}+2x_{Bj}\vec{P}=0$, where $\vec{q}$ and $\vec{P}$ are the momenta of the exchanged boson and the incoming proton) with cluster algorithms . They iteratively merge pairs of particles until only a few well separated objects are left. The decision to assign a given object to a jet is based on a distance measure (e.g. $k^2_{\perp i,j}$) and a resolution parameter y_{cut}. Three different types of $k_\perp$cluster jet algorithms are used:

- the longitudinally boost invariant $k_\perp$algorithm [33, 34],
- the $k_\perp$algorithm for DIS [10],
- the Cambridge algorithm [35] which we have adapted for DIS. In analogy to the prescription of the $k_\perp$ algorithm for DIS the proton remnant is treated as a pseudo-particle of infinite momentum.

Cone algorithms are not considered because of the ambiguities that arise in NLO calculations [2]. JADE algorithms are ignored for the various reasons explained in [9–11].

The longitudinally boost invariant $k_\perp$ jet algorithm defines jet events in an *inclusive* way. An event contains n hard jets plus an arbitrary number of particles that are not assigned to the hard jets, i.e. $ep \to e + n$ jets + anything. The $k_\perp$ algorithm for DIS and the Cambridge algorithm define *exclusive* jet events. Every particle in the event that is not clustered to the proton remnant is part of one of the jets, i.e. $ep \to e+(n+1)$ jets, where the (+1) stands for the proton remnant.

The parameters for the jet algorithms are chosen such that the total dijet cross sections are approximately of the same size:

$$\begin{array}{ll} \text{long. inv. } k_\perp: & E_{\perp\text{Breit},1} + E_{\perp\text{Breit},2} > 17\,\text{GeV} \quad \text{and} \quad E_{\perp\text{Breit},1,2} > E_{\perp\text{Breit,min}} = 5 \text{ GeV} \\ k_\perp \text{ and Cambridge}: & \dfrac{k^2_{\perp i,j}}{100 \text{ GeV}^2} > y_{cut} = 1 \quad \text{with} \quad k^2_{\perp i,j} = 2\min(E_i^2, E_j^2)(1-\cos\theta_{i,j}) \end{array} \tag{1}$$

$E_{\perp\text{Breit},1}$ and $E_{\perp\text{Breit},2}$ are the transverse momenta of the two highest $E_{\perp\text{Breit}}$ jets. $k_{\perp i,j}$ is a measure of the distance between particle i and j. y_{cut} is the resolution parameter.

For the longitudinally boost invariant $k_\perp$ jet algorithm the cut on $E_{\perp\text{Breit},1}+ E_{\perp\text{Breit},2}$ avoids the infrared sensitive region of phase space where both jets have similar $E_{\perp\text{Breit}}$ close to the minimal required $E_{\perp\text{Breit,min}}$ where perturbative calculations in fixed order α_s are not predictive [38]. The cuts used for the $k_\perp$ in DIS and the Cambridge jet algorithms ensure that the jets have $k_{\perp\text{Breit}} > 10$ GeV. This scenario leads to hard jets and intrinsically avoids the infrared sensitive regions.

The recombination of particles is done in the $E_\perp$-scheme according to the Snowmass convention [39] for the longitudinally boost invariant $k_\perp$ algorithm and in the E-scheme (addition of four-vectors) for the $k_\perp$ for DIS and the Cambridge jet algorithms. Only jets with $-1 < \eta_{jet,lab} < 2.5$, i.e. well within the detector acceptance, are selected.

The following differential cross sections are measured (the labels 1 and 2 refer to the two jets with the highest $E_{\perp\text{Breit}}$ in the event):

$$\begin{array}{l} \dfrac{d\sigma_{\text{dijet}}}{dQ^2}, \quad \dfrac{d^2\sigma_{\text{dijet}}}{dQ^2\, dx_{Bj}}, \\ \dfrac{d^2\sigma_{\text{dijet}}}{dQ^2\, d\bar{E}_{\perp\text{Breit}}} \quad \text{where} \quad \bar{E}_{\perp\text{Breit}} \equiv \dfrac{E_{\perp\text{Breit},1} + E_{\perp\text{Breit},2}}{2}, \\ \dfrac{d^2\sigma_{\text{dijet}}}{dQ^2\, dM_{jj}} \quad \text{where } M_{jj} \text{ is the invariant mass of the dijet system}, \\ \dfrac{d^2\sigma_{\text{dijet}}}{dQ^2\, d\xi} \quad \text{where} \quad \xi \equiv x_{Bj} \cdot \left(1 + \dfrac{M^2_{jj}}{Q^2}\right), \\ \dfrac{d^2\sigma_{\text{dijet}}}{dQ^2\, d\eta'}, \quad \dfrac{d^2\sigma_{\text{dijet}}}{d\bar{E}_{\perp\text{Breit}}\, d\eta'}, \quad \text{where} \quad \eta' \equiv \dfrac{|\eta_{1,Breit} - \eta_{2,Breit}|}{2}, \\ \dfrac{d^2\sigma_{\text{dijet}}}{dQ^2 d\eta_{\text{forward,lab}}}, \quad \dfrac{d^2\sigma_{\text{dijet}}}{dQ^2 d\eta_{\text{backward,lab}}}. \end{array} \tag{2}$$

$\eta_{\text{backward,lab}}$ and $\eta_{\text{forward,lab}}$ are the pseudorapidities of the backward and and the forward jet in the laboratory frame (with respect to the proton direction). The measurement is performed in the

[2] For details, see the discussion on the ad-hoc R_{sep} parameter [36, 37].

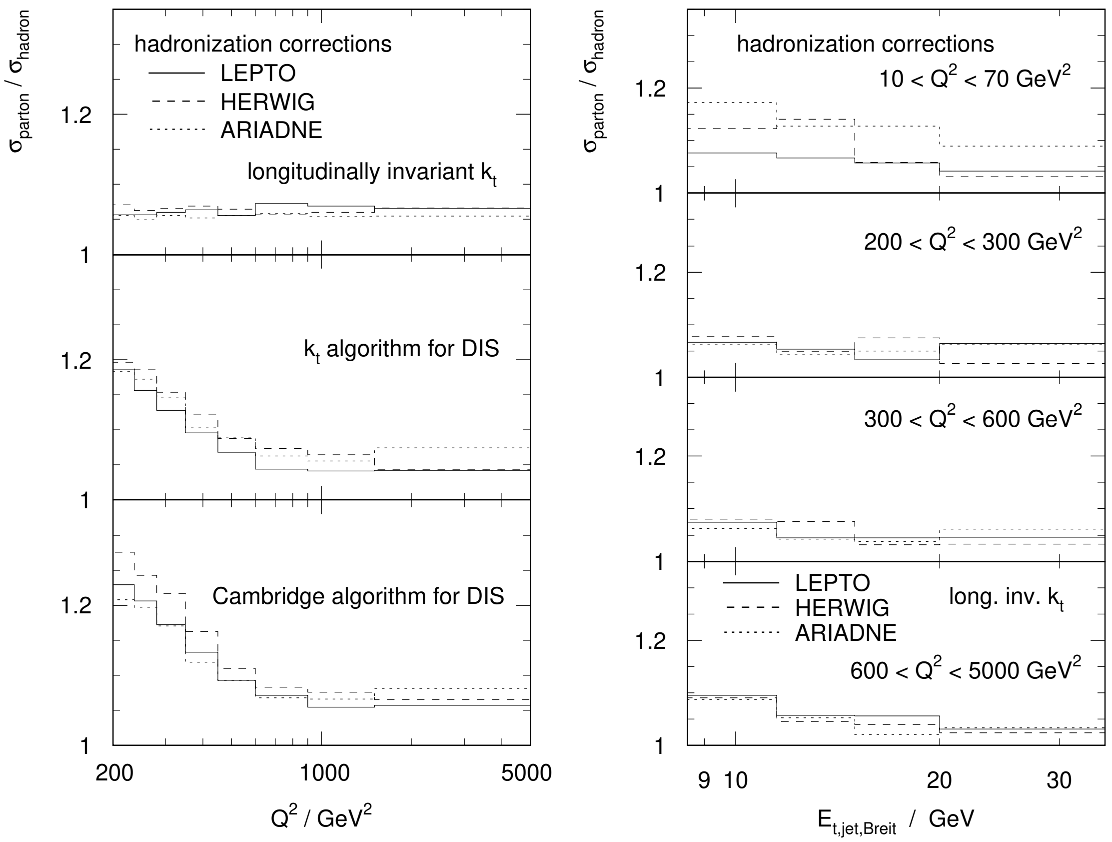

Figure 1: The hadronization corrections to the dijet cross sections, defined as the ratio of the cross section obtained with partons and with hadrons as predicted by models based on the Lund String model (LEPTO, ARIADNE) and on the cluster fragmentation model (HERWIG). Shown is the dependence on Q^2 for the different jet algorithms (left) and the $\bar{E}_{\perp\text{Breit}}$ dependence in bins of Q^2 for the longitudinally boost invariant $k_\perp$ algorithm (right).

phase space defined by

$$0.2 < y < 0.6\,,$$
$$10 < Q^2 < 70 \quad \text{and} \quad 200 < Q^2 < 5000\ \mathrm{GeV}^2\,. \tag{3}$$

The kinematic range is restricted to $Q^2 < 5000\ \mathrm{GeV}^2$. At larger values of Q^2 Z^0 exchange and γZ^0 interference terms start to contribute to the cross section. These effects are not included in the DISENT NLO calculation.

The jet selection criteria are chosen such that only hard jets are considered in the analysis. As a result the dijet cross sections are dominated by hard QCD processes and non-perturbative contributions are small. The hadronization corrections are defined as the ratio of the dijet cross sections before and after hadronization. Their size is estimated by the QCD models LEPTO, ARIADNE and HERWIG. In Fig. 1 (left) the Q^2 dependence of the hadronization corrections is shown for the different jet algorithms. All model predictions are in very good agreement. The longitudinally boost invariant $k_\perp$ algorithm has the smallest hadronization corrections among the jet algorithms under study. This algorithm is therefore taken as the central choice for the analysis at high Q^2. For this algorithm we extend the Q^2 range of the analysis down to values of $Q^2 = 10\,\mathrm{GeV}^2$. In Fig. 1 (right) we show the $\bar{E}_{\perp\text{Breit}}$ dependence of the hadronization corrections for $10 < Q^2 < 5000\,\mathrm{GeV}^2$. We observe a slight $\bar{E}_{\perp\text{Breit}}$ dependence of the corrections, which is more pronounced towards smaller values of Q^2 where the corrections and the model dependences are larger.

4 The H1 Detector

A detailed description of the H1 detector can be found elsewhere [40]. Here we briefly introduce the detector components relevant for this analysis: The liquid argon (LAr) calorimeter [41], the backward lead-scintillator calorimeter (BEMC) [42], and the tracking chamber system [43].

The hadronic energy flow is mainly measured by the LAr calorimeter extending over the polar angular range[3] $4.4° < \theta < 154°$ with full azimuthal coverage. It consists of an electromagnetic section ($20 - 30$ radiation lengths) with lead absorbers and a hadronic section with steel absorbers. The total depth of both calorimeters varies between 4.5 and 8 interaction lengths. Test beam measurements of the LAr calorimeter modules show an energy resolution of $\sigma_E/E \approx 0.50/\sqrt{E\ [\text{GeV}]} \oplus 0.02$ for charged pions [44]. The absolute scale of the hadronic energy is presently known to 4%, as determined e.g. from studies of the transverse momentum balance of the scattered positron and the hadronic final state in DIS events.

For $Q^2 > 100\ \text{GeV}^2$, the scattered positron is measured in the LAr calorimeter. Electromagnetic shower energies are measured with a resolution of $\sigma_E/E \approx 0.12/\sqrt{E\ [\text{GeV}]} \oplus 1\%$. These resolution were measured in test beam with electron energies between 5 and 166 GeV [45]. The uncertainty of the absolute electromagnetic energy scale has been determined by reconstructing the positron energies from the angle of the positron and the hadronic final state. It was found to be smaller than 3%.

For $5 \lesssim Q^2 \lesssim 100\ \text{GeV}^2$, the scattered positron is detected by the BEMC calorimeter with a depth of 22.5 radiation lengths covering the backward region of the detector, $151° < \theta < 176°$. The electromagnetic energy scale is known to an accuracy of 1%. The detectors in the backward region were upgraded in 1995. The BEMC calorimeter was replaced by the lead/scintillating fiber backward calorimeter SPACAL [46]. It covers the range $155° < \theta < 178°$.

The calorimeters are surrounded by a super-conducting solenoid providing a uniform magnetic field of 1.15 T parallel to the beam axis in the tracking region.

Charged particle tracks are measured in two concentric jet drift chamber modules (CJC), covering the polar angular range $15° < \theta < 165°$. A backward proportional chamber (BPC) with an angular acceptance of $155.5° < \theta < 174.5°$ serves to identify positrons.

5 Data Selection

At different Q^2 values the scattered positron is measured in different components of the H1 detector. The data are therefore split into two samples. The first sample consists of DIS events at "moderate" Q^2 ($10 < Q^2 < 100\ \text{GeV}^2$) where the scattered positron is detected in the BEMC calorimeter. The data have been taken in 1994 and correspond to an integrated luminosity of $\mathcal{L}_{int} \approx 2$ pb^{-1}. In the second sample the positron is scattered into the LAr calorimeter. This

[3]The polar angle θ is defined with respect to the proton beam direction ($+z$ axis).

results in $Q^2 > 200~\mathrm{GeV}^2$. These data at “high Q^2” have been taken in the year $1995 - 1997$ and correspond to an integrated luminosity of $\mathcal{L}_{int} \approx 34$ pb^{-1}.

At moderate Q^2 the scattered positron is measured well within the acceptance of the BEMC calorimeter at energies where trigger efficiencies are approximately 100%. To ensure a good identification of the scattered positron and suppress background from misidentified photoproduction events the following cuts are applied:

- The radial distance of the BPC space point has to be larger than 15 cm and moreover its x and y coordinate are required to be $x_{BPC} > 16$ cm or $y_{BPC} > 16$ cm
- The cluster of the positron candidate must have an energy-weighted mean transverse radius of $r_{\text{clust}} < 5$ cm.
- A BPC signal within 5 cm of the straight line connecting the electromagnetic shower center with the event vertex is required.

For the high Q^2 sample the selection of the scattered positron follows the procedure described in [47]. The events are triggered by requiring a localized energy deposition in the electromagnetic part of the LAr calorimeter. Within the acceptance region this trigger is fully efficient. The scattered positron candidate is required to have a compact electromagnetic cluster containing more than 98% of the LAr energy found within a pseudorapidity-azimuthal cone of opening $\sqrt{(\Delta\eta)^2 + (\Delta\phi)^2} = 0.25$. At least one track should have a distance of closest approach to the center of gravity of the cluster of less than 12 cm.

For both data samples the event vertex was required to be within 30 cm of the nominal position. The quantity $\sum(E - p_z)$ (the sum runs over all energy depositions in the calorimeter) is expected to be equal to twice the energy of the initial state positron. The cut $35\,\mathrm{GeV} < \sum(E - p_z) < 70\,\mathrm{GeV}$ reduces the contribution from photoproduction events as well as events where hard photons are radiated collinear to the incoming positron.

The event kinematics are calculated relying on the polar angle θ_{el} and the energy E'_{el} of the scattered positron via $Q^2_{el} = 2\,E_0\,E'_{el}\,(1 + \cos\theta_{el})$ and $y_{el} = 1 - \frac{E'_{el}}{2\,E_0}(1 - \cos\theta_{el})$. E_0 denotes the energy of the incoming positron. The DIS phase space is restricted to $y > 0.2$, since for lower cut values the event kinematics cannot be reconstructed from the scattered positron in a satisfactory way. The higher y cut avoids the region of low positron energies where the background from misidentified photoproduction events increases.

The jets are defined by the algorithms defined in section 3. The input for the jet algorithms consists of a combination of energy clusters from the calorimeter and track momenta measured in the central tracker. While the energy clusters are fully considered, the four momenta of each single track is only allowed to contribute up to a momentum of 350 MeV. This procedure partly compensates for expected energy losses in the calorimeter measurement (dead material, noise thresholds etc.). It reduces the dependence of the jet finding efficiency on the pseudorapidity of the jet and improves the resolution of the transverse jet energy [48].

As mentioned in section 3 the jets are required to be well within the acceptance of the LAr calorimeter. No extrapolation to regions beyond the detector acceptance is done. In addition to the jet selection cuts given in eq. (1) we also apply a cut on the jet energy in the laboratory frame $E_{jet,lab} > 4$ GeV. This cut only affects the tail of this distribution and removes badly measured jets at small energies.

In the moderate Q^2 sample 821 dijet events are selected with the longitudinally boost invariant $k_\perp$ algorithm. In the high Q^2 sample 2587 (long. inv. $k_\perp$), 2676 ($k_\perp$ for DIS), 2063 (Cambridge) dijet events are found.

The background from misidentified photoproduction events is estimated with a event sample generated with PHOJET [49] and is found to be negligible.

6 Correction of the Data

The data are corrected for detector effects and electroweak radiation from the initial and the final state lepton (corresponding to the level of stable hadrons)[4]. Both corrections are determined bin by bin.

The detector response is determined using events from Monte Carlo event generators including electroweak radiation that were subjected to a detailed simulation of the H1 detector. The hadronic final state of these events was modeled using either ARIADNE or LEPTO. To study radiation effects further independent event samples without the inclusion of electroweak corrections were generated.

Both QCD models give a very good description of the kinematical variables of the inclusive DIS data sample and quantities of the hadronic final state. Although both models do not describe the normalization of the dijet distributions, the shapes of transverse jet energies and jet rapidities are well described in both, the laboratory and the Breit frame.

The bin width of the observables has been chosen such that the bins are larger than the experimental resolution. To improve the resolution of the variable ξ the x_{Bj} and Q^2 values are, in this particular case, reconstructed by the sigma method [50].

For the high Q^2 data the total detector corrections are on average 5% (at most 15%) for the longitudinally boost invariant $k_\perp$ algorithm and the $k_\perp$ algorithm for DIS, while they are larger for the Cambridge algorithm (on average 15%, at most 25%). For $Q^2 > 20\ \mathrm{GeV}^2$ the average correction is 5% and at most 10%. For $Q^2 < 20\ \mathrm{GeV}^2$ the corrections are on average 20%. This somewhat large correction is due to the restricted acceptance in the BEMC calorimeter for the scattered positron and well understood.

All uncertainties are grouped into two classes: uncorrelated and correlated. Uncorrelated uncertainties are the statistical errors of the data and of the correction factors. Correlated uncertainties are the model dependence (spread) of the detector and radiative correction, variations of the cross section due to uncertainties of the hadronic energy scale (varied by $\pm 4\%$), the electromagnetic energy scale (BEMC positrons $\pm 1\%$, LAr positrons $\pm 3\%$), and uncertainties from the determination of the luminosity ($\pm 2.6\%$).

7 Dijet Cross Sections

7.1 Comparison of Data to NLO Predictions

The corrected differential cross sections are shown in Figs. 2 to 7. The inner errors of the data points show the quadratic sum of all uncorrelated uncertainties, while the outer error bars give the total uncertainties.

[4] We do not correct for the running of the electromagnetic coupling constant.

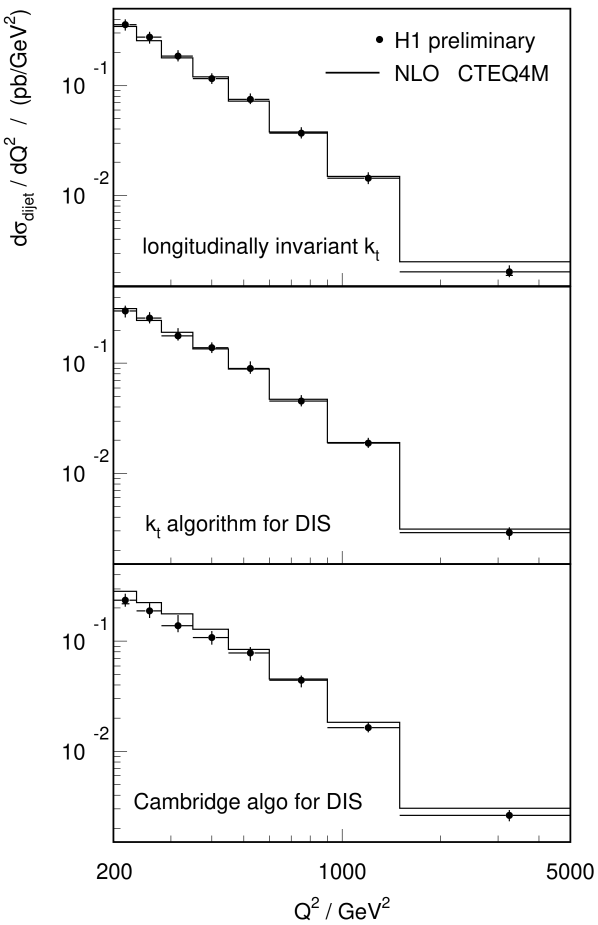

Figure 2: The Q^2 dependence of the dijet cross section for different jet algorithms for $200 < Q^2 < 5000\,\mathrm{GeV}^2$, compared to the NLO prediction of DISENT.

Since the hadronization corrections are relatively small (see Fig. 1), the corrected data are directly compared to the NLO predictions of DISENT. In all cases we use the CTEQ4M parton density functions [51] together with their corresponding value of $\alpha_s(M_z) = 0.116$ (2-loop formula). We have chosen a fixed factorization scale of the order of the average squared transverse jet energies $\mu_f^2 = 200\,\mathrm{GeV}^2 \simeq \langle \bar{E}^2_{\perp\mathrm{Breit}} \rangle$. However, the dependence of the NLO results on the choice of the factorization scale is very small.

The influence on the choice of the renormalization scale is significantly larger. Two natural candidates characterizing the hardness of the process are the transverse jet energy in the Breit frame $E_{\perp\mathrm{Breit}}$ (relevant in the limit $Q^2 \to 0$) and the virtuality of the exchanged photon Q^2 (relevant in the limit $E^2_{\perp\mathrm{Breit}} \to 0$). We compare the data to two NLO calculations with both choices $\mu_r^2 = Q^2$ and $\mu_r^2 = Q^2 + E^2_{\perp\mathrm{Breit}}$. The latter choice is preferable since it gives a smooth interpolation between both limits. Differences between the two choices are however only visible at relatively low Q^2.

In Fig. 2 we show the Q^2 distribution (for $Q^2 > 200\ \mathrm{GeV}^2$) for the three different jet algorithms. For all jet algorithms we see a good description of the data by the NLO prediction. Only for the Cambridge algorithm a small discrepancy is seen. However, the Cambridge algorithm has larger hadronization corrections, which are approximately of the same size as the observed discrepancy. We conclude that for these jet algorithms the agreement between data and theory does not depend on details in the jet definition.

For the longitudinally boost invariant $k_\perp$ algorithm the Q^2 range is extended down to $10\,\mathrm{GeV}^2$

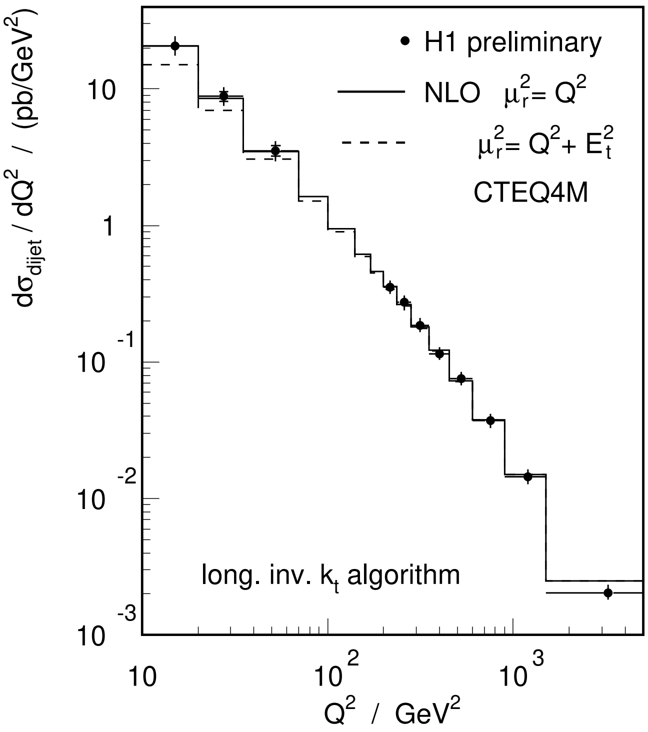

Figure 3: The Q^2 dependence of the dijet cross section for the longitudinally boost invariant $k_\perp$ algorithm for $10 < Q^2 < 5000\,\mathrm{GeV}^2$, compared to the NLO predictions for different choices of the renormalization scale.

(see Fig. 3). While at large Q^2 the NLO results for both renormalization scales agree, they show larger differences (up to 30%) in this Q^2 region. We observe that only for the choice $\mu_r^2 = Q^2$ the data are described by the NLO predictions.

In Fig. 4 the measured cross sections are displayed double differentially in Q^2 and in $E_{\perp\mathrm{Breit}}$ (left) and in the invariant dijet mass M_{jj} (right). The spectra of both distributions become harder with increasing Q^2. Again, both distributions are well described by NLO for the choice $\mu_r^2 = Q^2$. Here we see that the relative differences in the NLO calculations for both renormalization scales are almost independent of $E_{\perp\mathrm{Breit}}$ and M_{jj}, but only depend on Q^2.

Comparisons of data to NLO predictions are shown in Figs. 5 to 7 for ξ, x_{Bj}, η', $\eta_{lab,forward}$, $\eta_{lab,backward}$. In nearly all distributions under study the discrepancies between data and the NLO prediction for the choice $\mu_r^2 = Q^2 + E_{\perp\mathrm{Breit}}^2$ at $Q^2 < 70\,\mathrm{GeV}^2$ are not seen in the shape but only in the overall normalization. Only in the pseudorapidity distributions of the jets in the laboratory frame (Fig. 7) we do observe a dependence of the shapes on the choice of the renormalization scale.

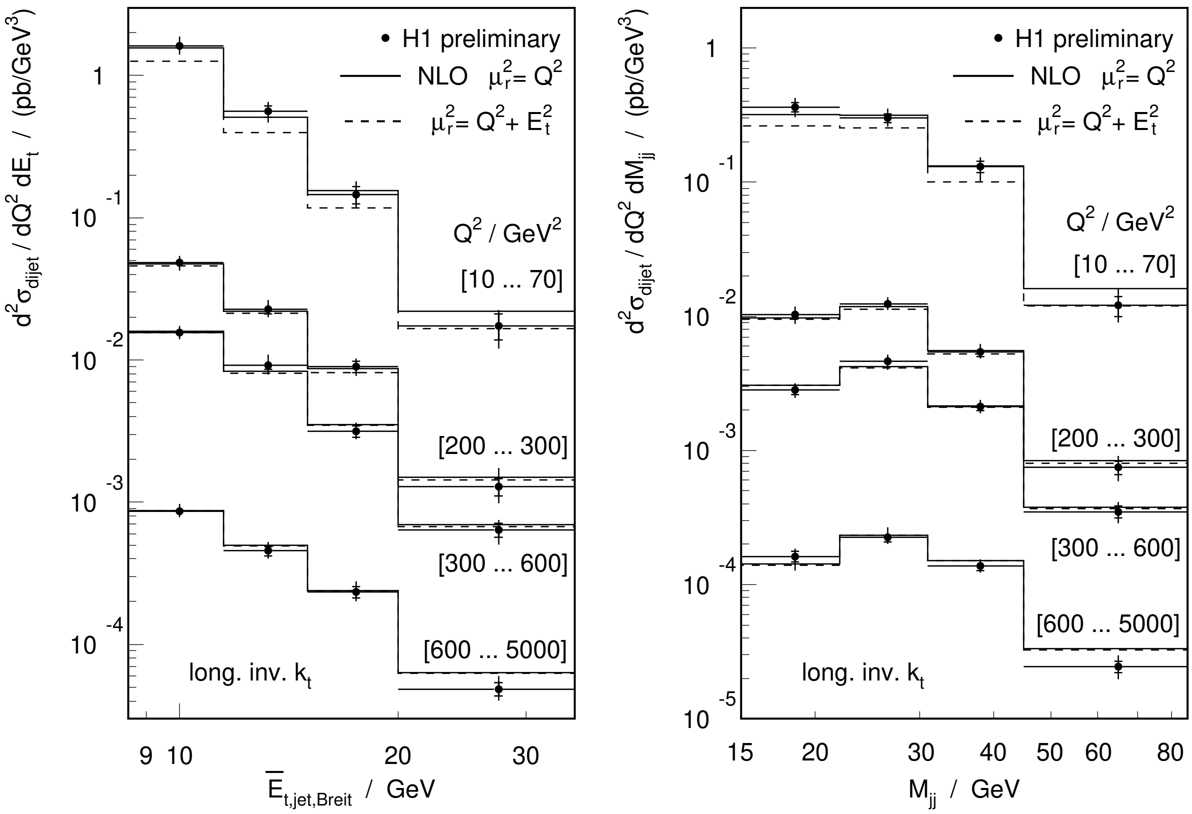

Figure 4: Dijet cross sections double differentially in Q^2 and the average transverse jet energy in the Breit frame (left) and the invariant dijet mass (right) in Q^2 bins. The data are compared to the NLO predictions for two different renormalization scales.

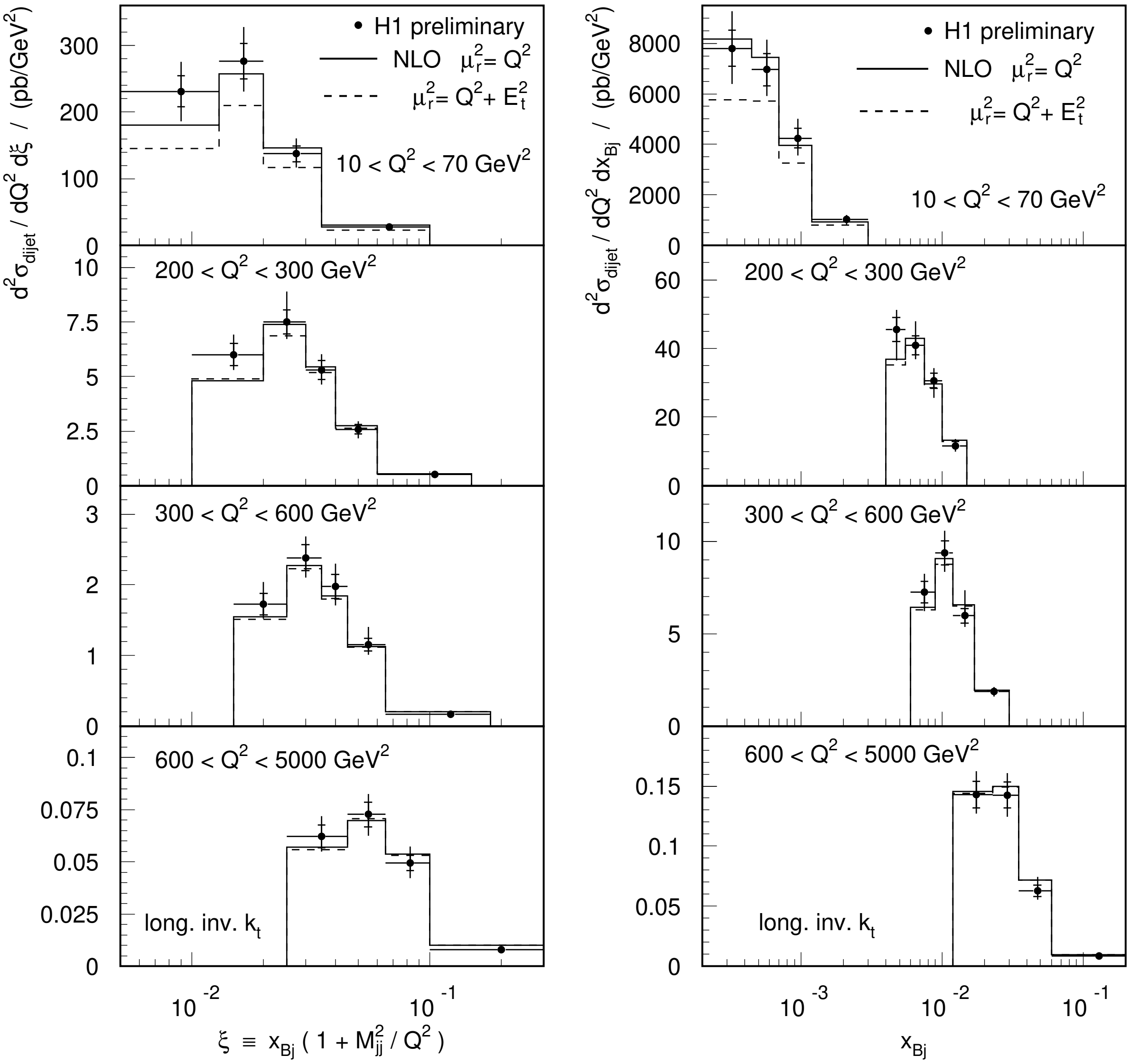

Figure 5: Dijet cross sections double differentially in Q^2 and the kinematic variables ξ (left) and x_{Bj} (right). The data are compared to the NLO predictions for two different renormalization scales.

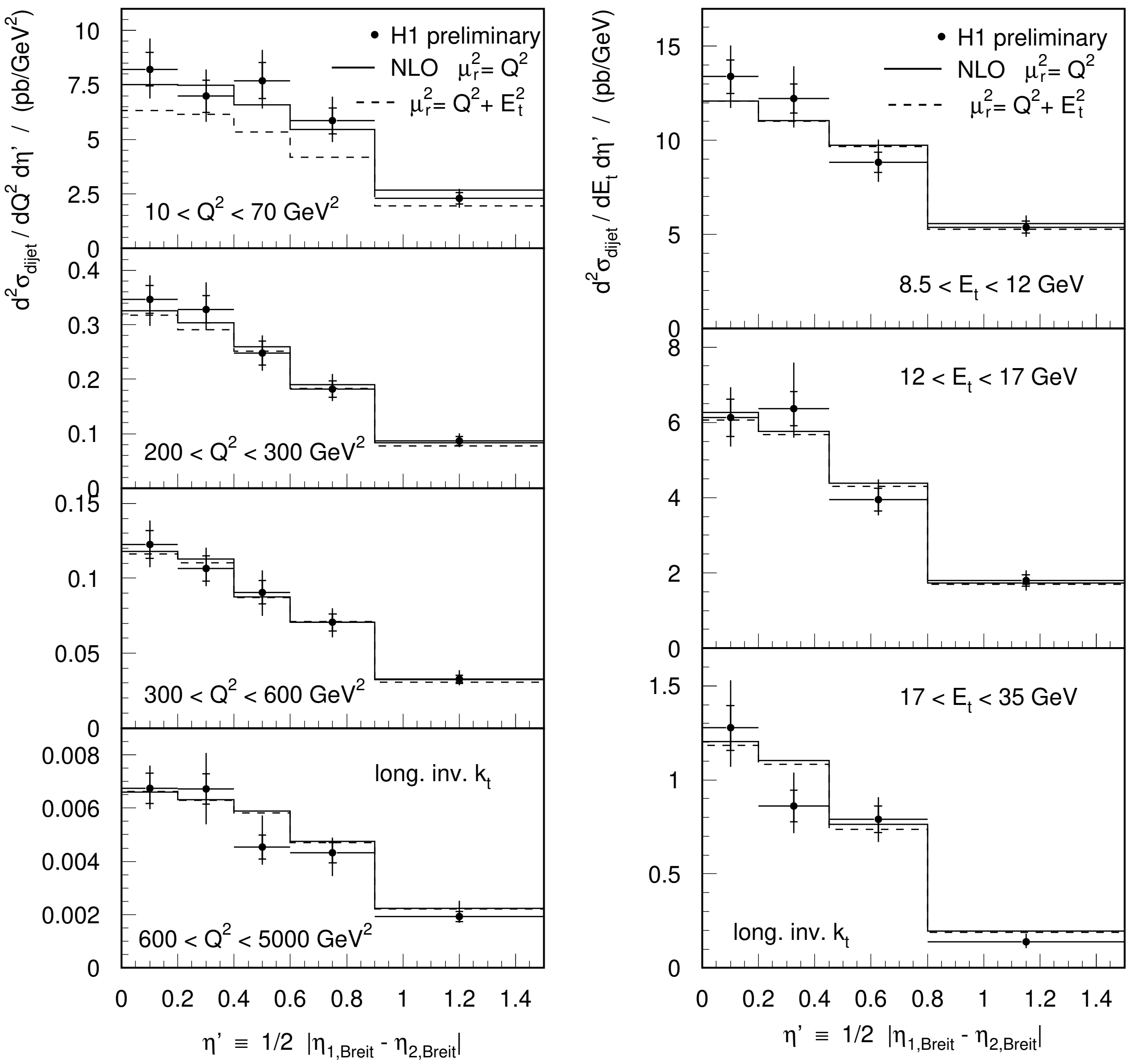

Figure 6: The η' dependence of the dijet cross sections double differentially in Q^2 (left) and in E_t (right) – the latter only for $Q^2 > 200$ GeV^2. The data are compared to the NLO predictions for two different renormalization scales.

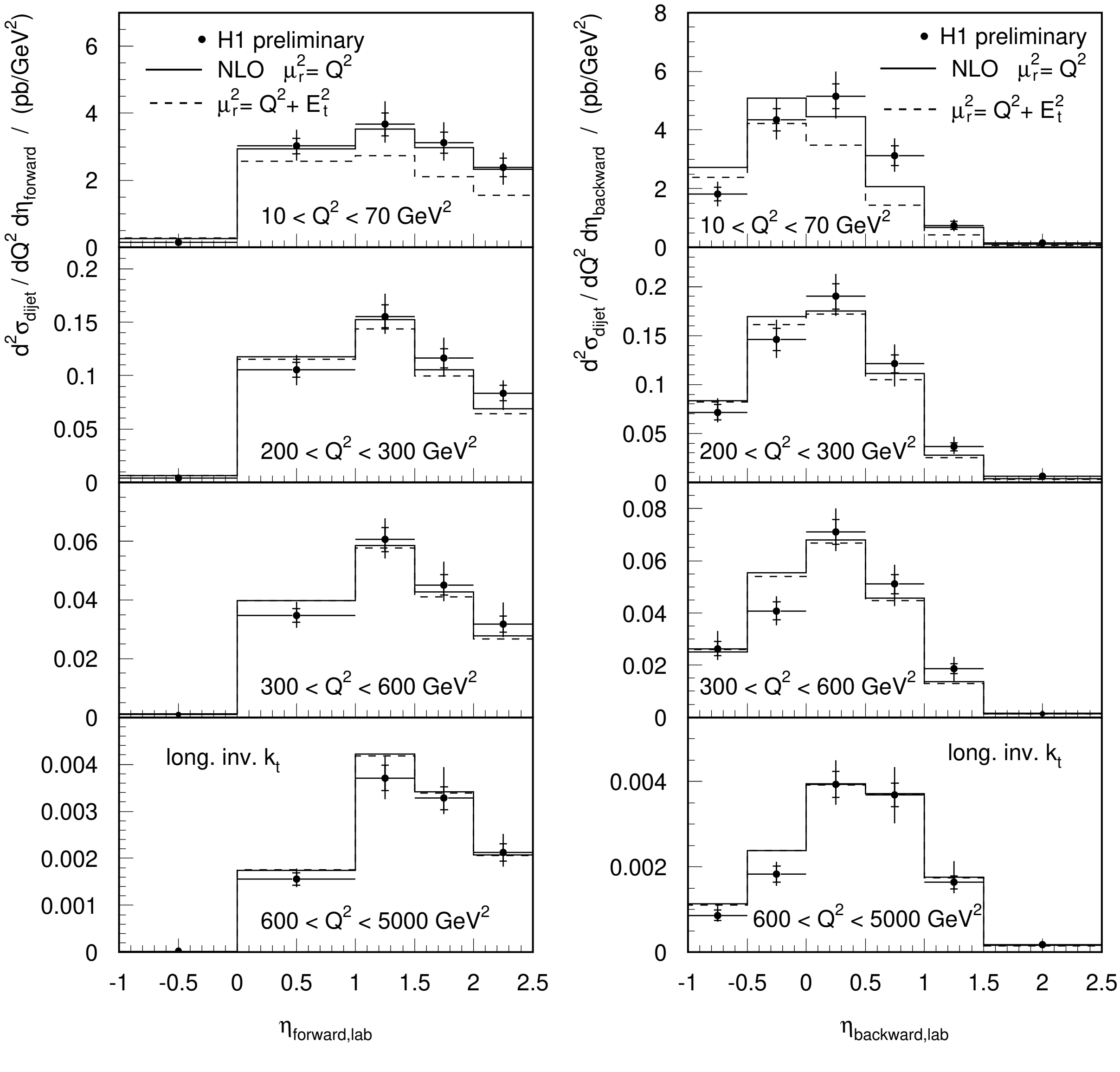

Figure 7: Jet pseudorapidity distributions in the laboratory frame for the forward (left) and backward jet (right) in different Q^2 regions. The data are compared to the NLO predictions for two different renormalization scales.

8 Direct Determination of the Gluon Density in the Proton

In this section we present a direct determination of the gluon density in the proton from a QCD fit to the measured dijet cross sections. The fit is performed to the dijet cross sections $\mathrm{d}^2\sigma/(\mathrm{d}Q^2\mathrm{d}\xi)$ and $\mathrm{d}^2\sigma/(\mathrm{d}Q^2\mathrm{d}x_{Bj})$ (see Fig. 5). The ξ and x_{Bj} distributions are most sensitive to the x-dependence of the parton densities[5]. For the longitudinally boost invariant $k_\perp$ algorithm at $200\ \mathrm{GeV}^2 < Q^2 < 5000\ \mathrm{GeV}^2$ the hadronization corrections are smallest (approx. 7%) and flat in the Q^2, ξ, x_{Bj} distributions, while for the other jet algorithms these corrections are substantially larger and show a strong dependence on these quantities. Furthermore the theoretical scale uncertainties are significantly smaller for $Q^2 > 200\,\mathrm{GeV}^2$ compared to the dijet cross sections at smaller Q^2.

The dijet cross section in this kinematic range receives contributions from partons with a fractional proton momentum $0.01 \lesssim x \lesssim 0.2$. The dijet cross section is directly sensitive to the gluon density as well as to the quark densities in the proton. To have independent constraints on the quark densities in the QCD fit we also include recent H1 data [47] on the inclusive neutral current DIS ep-cross section ("inclusive DIS cross sections", σ^{incl}) at $200 \le Q^2 \le 650\,\mathrm{GeV}^2$ and $0.005 \le x_{Bj} \le 0.65$ in the fit. These data give strong constraints on the quark densities in the x range under consideration while they are less sensitive to the gluon density. This procedure considers the correlation between quark and gluon densities in the QCD fit in a consistent way.

Using these data sets we perform a QCD fit and extract the gluon density and the quark densities in the proton at a factorization scale $\mu_f^2 = 200\,\mathrm{GeV}^2$ in the range $0.01 < x < 0.1$, without relying on any further assumptions (inclusion of additional data sets, evolution of parton densities, sum rules). The only additional input is the value of the strong coupling constant which is taken as the world average with its corresponding uncertainty $\alpha_s(M_Z^2) = 0.119 \pm 0.005$ [52].

8.1 Cross Sections in Perturbative QCD

In perturbative QCD the cross section of a deep-inelastic lepton proton scattering process can be written as a convolution of the perturbative coefficients c_a with the (non-perturbative) parton densities $f_{a/p}$ in the proton

$$\sigma_{\text{proc.}} = \sum_{a,n} \int_0^1 dx\ \alpha_s^n(\mu_r^2)\ c_{a,n}^{\text{proc.}}(\mu_r^2, \mu_f^2)\ f_{a/p}(x, \mu_f^2)\,. \tag{4}$$

The summation is performed over all contributing parton flavours a and all orders n of the strong coupling constant considered in the perturbative calculation. However, the coefficients c_a for the different parton flavours are not all independent. Neglecting parton masses, for photon induced processes (i.e. neglecting contributions from Z^0 exchange) the following relations are valid

$$c_u = c_c = c_t \ = \ c_{\bar u} = c_{\bar c} = c_{\bar t} \qquad \text{and} \qquad c_d = c_s = c_b \ = \ c_{\bar d} = c_{\bar s} = c_{\bar b}\,. \tag{5}$$

[5]The variable x is used here to denote the fractional longitudinal momentum of the proton carried by the parton. Beyond leading order this variable is only defined within a given theoretical frame (factorization scheme and scale) and is not an observable quantity. To distinguish it from the Bjorken scaling variable, the latter is throughout labeled with an index: x_{Bj}.

Only three coefficients are therefore independent, which can be written as linear combinations of the single flavour coefficients

$$c_G = c_{gluon} \; , \qquad c_\Delta = 3\,(c_u - c_d) \; , \qquad c_\Sigma = 1/3\;(4\,c_d - c_u) \; . \tag{6}$$

The linear combinations of the quark densities $\Delta(x), \Sigma(x)$ that correspond to the coefficients c_Δ, c_Σ are given by

$$\begin{aligned} \Delta(x) &= \sum_i e_i^2\;(q_i(x) + \bar{q}_i(x)) \; , \\ \Sigma(x) &= \sum_i (q_i(x) + \bar{q}_i(x)) \; , \end{aligned} \tag{7}$$

where the sum runs over all quark flavours i and e_i is the electrical charge of the quarks. The gluon gives contributions to the ep-cross section at $\mathcal{O}(\alpha_s^1)$ and higher. In $\mathcal{O}(\alpha_s^0)$ and $\mathcal{O}(\alpha_s^1)$ the coefficients fulfill $c_u = 4\,c_d$, so the quarks contribute only via the $\Delta(x)$. At order $\mathcal{O}(\alpha_s^2)$ also the $\Sigma(x)$ starts to contribute. Up to NLO the inclusive neutral current DIS ep-cross section σ^{incl} and the dijet cross section σ^{dijet} have the following contributions

	LO	NLO
σ^{incl}	$\Delta(x)$	$\Delta(x), G(x)$
σ^{dijet}	$G(x), \Delta(x)$	$G(x), \Delta(x), \Sigma(x)$

The contribution of the $\Sigma(x)$ to the NLO dijet cross section for CTEQ4M parton densities is as small as 2.6%. We therefore fit the gluon and the quark densities ($G(x), \Delta(x)$) to our measurements of σ^{incl} and σ^{dijet} while we take the $\Sigma(x)$ from CTEQ4M [51], MRST [53] or GRV94HO [54].

8.2 The NLO QCD fit

To fit the data to the theoretical predictions we perform a χ^2 minimization using the MINUIT program [55]. The definition of χ^2 fully takes into account all correlations of systematic uncertainties between the data points (as described in [56]). The inclusive DIS cross section data are compared to the NLO predictions, and the dijet data are compared to the product of the NLO prediction and the hadronization correction (as defined in section 3)

$$\begin{aligned} \sigma_{H1}^{\text{incl}} &\leftrightarrow \sigma_{NLO}^{\text{incl}}(G(x),\,\Delta(x))\,, \\ \sigma_{H1}^{\text{dijet}} &\leftrightarrow \sigma_{NLO}^{\text{dijet}}(G(x),\,\Delta(x))\,\cdot\,c_{\text{hadronization}}^{-1} \qquad \text{where} \qquad c_{\text{hadronization}} = \frac{\sigma_{\text{parton}}}{\sigma_{\text{hadron}}}\,. \end{aligned}$$

The value of the hadronization correction is taken as the mean value of the LEPTO, ARIADNE and HERWIG predictions, which are always in agreement within two percent. We investigated the dependence of these corrections on model parameters in LEPTO and in JETSET by varying them in the ranges described in [7, 8] and found no changes above 3%. The final hadronization corrections for the ξ and the x_{Bj} distributions for the longitudinally boost invariant $k_\perp$ algorithm are between 4% and 8% with an assumed uncertainty of $\pm 3\%$.

During the fit the calculation of the NLO cross sections has to be repeated many times. Since standard computations of NLO cross sections are time-consuming we use a method similar to the one proposed in [57] for the fast reevaluation of the NLO cross sections[6]. All NLO calculations are performed in the $\overline{MS}$ scheme for five massless quark flavours using the DISENT program. The renormalization and factorization scales in the NLO calculations are set to

$$
\begin{array}{lll}
\sigma^{\text{incl}}: & \mu_r^2 = Q^2 & \mu_f^2 = 200\,\text{GeV}^2 \quad (\simeq Q^2) \quad , \\
\sigma^{\text{dijet}}: & \mu_r^2 = Q^2 + \bar{E}^2_{\perp\text{Breit}} & \mu_f^2 = 200\,\text{GeV}^2 \quad (\simeq \langle \bar{E}^2_{\perp\text{Breit}} \rangle) \quad .
\end{array}
$$

The value of the strong coupling constant at a scale μ_r^2, relative to its value at $\mu_r^2 = M_Z^2$ is given by the 2-loop formula.

The choice of the fixed value of the factorization scale (which is for both processes approximately equal to the hard scale) allows to determine the gluon and the quark densities at this scale without relying on additional assumptions on the evolution.

The x-dependences of the gluon and the quark densities are parameterized using the functions

$$
\begin{array}{lrcl}
\text{3-parameter:} & xP(x) & = & A\, x^b\, (1-x)^c \,, \\
\text{4-parameter:} & xP(x) & = & A\, x^b\, (1-x)^c\, (1 + dx) \,, \\
\text{5-parameter:} & xP(x) & = & A\, x^b\, (1-x)^c\, (1 + d\sqrt{x} + ex) \,,
\end{array}
\tag{8}
$$

where $xP(x)$ stands for one of $xG(x)$ and $x\Delta(x)$. These forms are usually used to parameterize the x-dependence of parton distributions at small scales ($\mu_f^2 \approx 4\,\text{GeV}^2$). To see that these parameterizations are still flexible enough to describe the parton behaviour at $\mu_f^2 = 200\,\text{GeV}^2$ we have checked that they are able to describe the gluon and the $\Delta(x)$ distributions from global fits (CTEQ4M, MRST, GRV94HO) at $\mu_f^2 = 200\,\text{GeV}^2$ within one or two percent. The final results are obtained with the 3-parameter (5-parameter) ansatz for the gluon (quark $\Delta(x)$) density. However, changing both to the 4-parameter ansatz has no influence on the fit results.

The uncertainties due to the choice of the renormalization and the factorization scale in the NLO calculation are estimated by independent variations of these scales $\mu^2_{r,f}$ by a factor of four around the central choice (μ_0^2). In each case we calculate the relative change of the NLO cross section using the CTEQ4M parton distribution $\frac{\tilde{\sigma}_{NLO}(x_\mu \cdot \mu_0^2)}{\tilde{\sigma}_{NLO}(\mu_0^2)}$, where $x_\mu = \{\frac{1}{4}, 4\}$. We redo the fit, replacing $\sigma_{NLO}(\mu_0^2)$ by $\sigma_{NLO}(\mu_0^2) \cdot \frac{\tilde{\sigma}_{NLO}(x_\mu \cdot \mu_0^2)}{\tilde{\sigma}_{NLO}(\mu_0^2)}$. The resulting deviations from the central fit result are added in quadrature to the error band that contains all experimental uncertainties, the uncertainties of the hadronization corrections and the uncertainty of $\Delta\alpha_s(M_Z^2) = \pm 0.005$.

The total number of data points included in the fit is 73 (inclusive DIS cross sections: 47, dijet cross sections: 26). The number of fit parameters is eight (five for the quark $\Delta(x)$ and three for the gluon). The fit gives a χ^2/Ndof $\simeq 0.58$. The χ^2 values for the single data points for the inclusive DIS cross sections and the dijet cross sections are of equal size.

The stability of the fit result is tested by the following variations:

- We investigate that dijet data do not influence the fit results of the quark $\Delta(x)$ density by performing the fit of the $\Delta(x)$ with and without the dijet cross sections included. On the other hand we observe that the inclusive DIS cross sections (in the range considered here) are completely insensitive to the gluon density. The gluon contribution to these cross sections is at most 5% (the gluon contribution to the dijet cross section is on average 56%). This means that the quark $\Delta(x)$ is determined by the inclusive DIS cross section data while the gluon density is fixed by the dijet cross sections.

[6]The computation of the NLO dijet cross section with the high statistics used in our QCD fit takes more than 100 hours on a SUN workstation. For the calculation of the final error band approx. 20,000 calculations are needed.

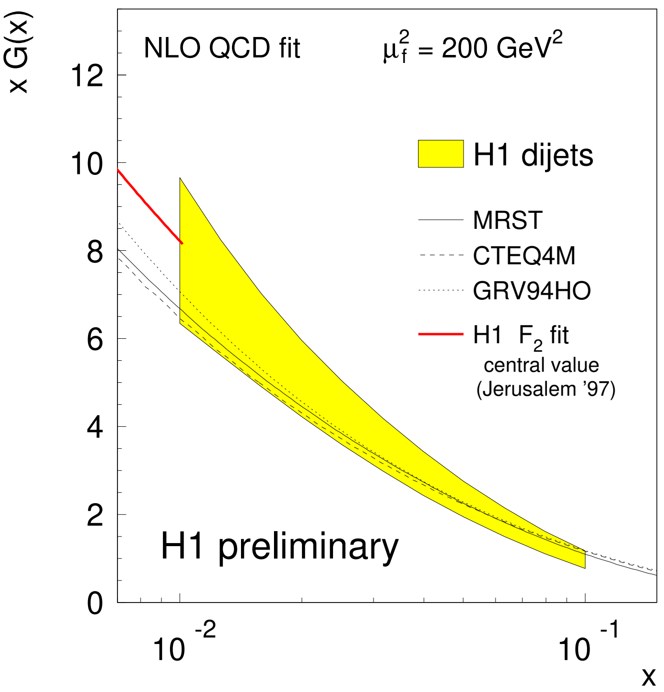

Figure 8: The gluon density in the proton from a NLO QCD fit to dijet cross sections, obtained for a value of $\alpha_s(M_Z^2) = 0.119 \pm 0.005$. The error band is compared to the gluon densities obtained in different global analyses and to the result from a fit to H1 structure function data (only to the central value without error band).

- We repeat the fits using different parameterizations for the gluon ($3 \to 4$ parameter) and the quark $\Delta(x)$ ($5 \to 4$ parameter) and see that the results do not depend on these choices.
- The quark $\Sigma(x)$ distribution in the central fit is taken from the CTEQ4M parameterization. Replacing this by the parameterizations from MRST or GRV94HO has no influence on the results, which is, of course, expected since the $\Sigma(x)$ contribution is so small (only $\approx 2.6\%$ for the dijets).
- Instead of fitting the ξ and the x_{Bj} cross sections we fit other dijet distributions ($\bar{E}_{\perp\mathrm{Breit}}$, M_{jj}, η') and combinations of these and (ξ, x_{Bj}). All of these fit results are compatible with the central result.
- We extend the Q^2 range of the fitted data by subsequently including data towards lower Q^2 values down to $Q^2 = 10\,\mathrm{GeV}^2$. In all cases the results are consistent with the result, obtained by fitting only high Q^2 data. Although the inclusion of this data leads to a resulting gluon density that is slightly higher than the central result, it has to be pointed out that theoretical uncertainties are much larger in this phase space. Furthermore one has to consider that we may expect additional contributions from resolved photon processes at $Q^2 \approx 10\,\mathrm{GeV}^2$ which are not included in our NLO calculation.

8.3 Fit results

The quark $\Delta(x)$ density resulting from the fit is approx. 5% higher at $x = 0.01$ compared to the results of the global fits (CTEQ4M, MRST, GRV94HO) while it is in good agreement at $x = 0.1$.

The result for the gluon density is shown in Fig. 8: The error band of the gluon density from the fit to the dijet cross sections and the inclusive DIS cross sections at a factorization scale $\mu_f^2 = 200\,\mathrm{GeV}^2$ in the range $0.01 < x < 0.1$. The result is compared to the results from various global analyses and to the gluon density determined from H1 structure function data (the result from [58], evolved to $\mu_f^2 = 200\,\mathrm{GeV}^2$ – only the central value is shown without error band).

While the determined gluon density is slightly higher than the results from the global analyses (although compatible within the error) it is in good agreement with the gluon density from the QCD analysis of the H1 F_2 data at $x = 0.01$.

9 Summary

Measurements of dijet cross sections in DIS over a large kinematic range of Q^2 ($10 < Q^2 < 5000\,\mathrm{GeV}^2$) at transverse jet energies ($70 \lesssim E^2_{\perp\mathrm{Breit}} \lesssim 1200\,\mathrm{GeV}^2$) are presented. The corrected dijet cross section as a function of Q^2 has been measured for three different $k_\perp$ cluster jet algorithms. For all jet algorithms good agreement with the NLO predictions is found.

The longitudinally boost invariant $k_\perp$ algorithm shows significantly smaller hadronization corrections than the other jet algorithms. Therefore it is used to measure the double differential dijet cross sections for Q^2, x_{Bj}, $\bar{E}_{\perp\mathrm{Breit}}$, ξ, η', $\eta_{lab,forward}$ and $\eta_{lab,backward}$.

NLO calculations give a good description of the dijet data over nearly four orders of magnitude in Q^2, three orders in x_{Bj}, nearly two orders in ξ, and more than one order in $E^2_{\perp\mathrm{Breit}}$ and the invariant dijet mass M^2_{jj}. For $Q^2 < 70\ \mathrm{GeV}^2$, however, NLO corrections are very large and the dependence of the theoretical predictions on the renormalization scale in the NLO calculation is large.

At higher momentum transfers ($Q^2 > 200\ \mathrm{GeV}^2$) NLO corrections are small and the NLO prediction is stable with respect to the choice of the renormalization and factorization scales. In this kinematic range we perform a NLO QCD fit to these dijet cross sections. Including recent H1 neutral current inclusive DIS cross sections measurements to fix the quark contributions, we fit the gluon density to the dijet cross sections in the range $0.01 < x < 0.1$ at a factorization scale $\mu_f^2 = 200\,\mathrm{GeV}^2$ for a given value of $\alpha_s(M_Z) = 0.119 \pm 0.005$.

The gluon density determined in dijet production in DIS extends the x-range from previous determinations from H1 structure function data to larger x-values. While the resulting gluon density is slightly higher than the results from the global analyses (although compatible within the error) it is in good agreement with the gluon density from the QCD analysis of the H1 F_2 data. The agreement between the gluon density extracted from the scaling violation of the structure function F_2 and from the direct determination in high $E_\perp$ dijet production clearly demonstrates the universality (i.e. the process independence) of the gluon density.

Acknowledgments

We are grateful to the HERA machine group whose outstanding efforts have made and continue to make this experiment possible. We thank the engineers and technicians for their work in constructing and now maintaining the H1 detector, our funding agencies for financial support, the DESY technical stuff for continual assistance, and the DESY directorate for the hospitality which they extend to the non-DESY members of the collaboration. We also wish to thank E. Mirkes, B. Pötter, M. H. Seymour and D. Zeppenfeld for many helpful discussions.

References

[1] D. Graudenz, Phys. Lett. B 256 (1992) 518; Phys. Rev. D 49 (1994) 3291; Comp. Phys. Comm. 92 (1995) 65.

[2] T. Brodkorb and J. G. Körner, Z. Phys. C 54 (1992) 519; T. Brodkorb and E. Mirkes, Z. Phys. C 66 (1995) 141.

[3] JADE Collab., W. Bartel et al., Z. Phys. C33 (1986) 23.

[4] D. Graudenz and N.Magnussen, Proceedings of the workshop physics at HERA, Hamburg, Germany, eds. W. Buchmüller and G. Ingelman Vol.1 (1991) 261.

[5] H1 Collab., T. Ahmed et al., Phys. Lett. B 346 (1995) 415.

[6] ZEUS Collab., M. Derrick et al., Phys. Lett. B 363 (1995) 201.

[7] H1 Collab., C. Adloff et al., abstract 527 submitted to this conference.

[8] H1 Collab., C. Adloff et al., DESY-98-075 Hamburg, Germany, submitted to Eur. Phys. J. C, abstract 528 submitted to this conference.

[9] N. Brown and W.J. Stirling, Phys.Lett. B 252 (1990) 657.

[10] S. Catani, Yu.L. Dokshitzer and B.R. Webber, Phys. Lett. B 285 (1992) 291.

[11] B.R. Webber, J. Phys. G 19 (1993) 1567.

[12] E. Mirkes and D. Zeppenfeld, Phys. Lett. B380 (1996) 205.

[13] S. Catani and M.H. Seymour, Nucl. Phys. B 485 (1997) 291, Erratum-ibid. B 510 (1997) 503.

[14] D. Graudenz, (Oct 1997) hep-ph/9710244.

[15] B. Pötter, DESY-98-071, Hamburg, Germany (Jun 1998) and hep-ph/9806437.

[16] CDF Collab., F. Abe et al., Phys. Rev. D 45 (1992) 1448 and L.A. del Pozo PhD Thesis University of Cambridge, RALT-002, 1993.

[17] H1 Collab., C. Adloff et al., DESY-98-076 Hamburg (Germany), submitted to Eur. Phys. J. C and abstract 523 submitted to this conference.

[18] G. Ingelman, A. Edin and J. Rathsman, Comp. Phys. Comm. 101 (1997) 108, Version used: 6.5.

[19] M. Bengtsson and T. Sjöstrand, Z. Phys. C 37 (1998) 465; Sjöstrand, Proc. of the HERA workshop 1987, Hamburg Vol. 1 (1988) 149.

[20] V.N. Gribov and L.N. Lipatov, Sov. J. Nucl. Phys. 15 (1972) 438 and 675; Yu. L. Dokshitzer, Sov. Phys. JETP 46 (1977) 641; G. Altarelli and G. Parisi, Nucl. Phys. 126 (1977) 297.

[21] B. Andersson et al., Phys. Rep. 97 (1983) 31.

[22] T. Sjöstrand, Comp. Phys. Comm. 39 (1986) 347; T. Sjöstrand and M. Bengtsson, ibid. 43 (1987) 367.

[23] G. Marchinesi et al., Comp. Phys. Comm. 67 (1992) 465, version used: 5.9.

[24] M.H. Seymour, Nucl. Phys. B 436 (1995) 443.

[25] B.R. Webber, Nucl. Phys. B 238 (1984) 492.

[26] L. Lönnblad, Comp. Phys. Comm. 71 (1992) 15, Version used: 4.08.

[27] G. Gustafson and Ulf Petterson, Nucl. Phys. B 306 (1988); G. Gustafson, Phys. Lett. B 175 (1986) 453; B. Andersson, G. Gustafson, L. Lönnblad and Ulf Petterson, Z. Phys. C 43 (1989) 625.

[28] L. Lönnblad, Z. Phys. C 65 (1995) 285.

[29] K. Charchula, G. Schuler and H. Spiesberger, Comp. Phys. Comm. 81 (1994) 381.

[30] A. Kwiatkowski, H. Spiesberger and H.-J. Möhring, Comp. Phys. Comm. 69 (1992) 155.

[31] E. Mirkes and D. Zeppenfeld, Proceedings of the workshop on deep-inelastic scattering and QCD (DIS97), eds. D. Krakauer and J. Repond, Chicago, Illinois (1997).

[32] B. Pötter, Proceedings of the workshop on deep-inelastic scattering and QCD (DIS98), eds. R. Roosen and P. Marage, Brussels, Belgium (1998) and hep-ph/9805436.

[33] S.D. Ellis and D.E. Soper,, Phys. Rev. D 48 (1993) 3160.

[34] S. Catani, Yu.L. Dokshitzer, M.H. Seymour and B.R. Webber, Nucl. Phys. B 406 (1993) 187.

[35] Yu.L. Dokshitzer, G.D. Leder, S. Moretti and B.R. Webber, J. High Energy Phys. 08 (1997) 1.

[36] M.H. Seymour, in: Rencontres de Moriond, Les Arcs, France (1998) and hep-ph/9807226.

[37] M. Klasen and G. Kramer, Phys. Rev. D56 (1997) 2702.

[38] S. Frixione and G. Ridolfi, Nucl. Phys. B 507 (1997) 315.

[39] J. Huth et al., Proceedings of the summer study on high energy physics, Snowmass, Colorado (1990) 134.

[40] H1 Collaboration, I. Abt et al., Nucl. Instr. and Meth. A 386 (1997) 310 and 348.

[41] H1 Calorimeter Group, B. Andrieu et al., Nucl. Instr. and Meth. A 336 (1993) 460.

[42] H1 BEMC Group, J. Bán et al., Nucl. Instr. and Meth. A 372 (1996) 399.

[43] J. Bürger et al., Nucl. Instr. Meth. A 279 (1989) 217; H1 FTD group, S. Burke et al., Nucl. Instr. Meth. A 313 (1996) 373.

[44] H1 Calorimeter Group, B. Andrieu et al., Nucl. Instr. and Meth. A 372 (1996) 399.

[45] H1 Calorimeter Group, B. Andrieu et al., Nucl. Instr. and Meth. A 344 (1994) 492.

[46] H1 SPACAL Group, R. D. Appuhn et al., Nucl. Instr. and Meth. A 386 (1997) 397.

[47] H1 Collab., contributed paper 262 to ICHEP 97, Jerusalem, Israel (1997).

[48] J. Spiekermann, Ph. D. Thesis, University of Dortmund, unpublished; H. Rick, Ph. D. Thesis, University of Dortmund, unpublished.

[49] R. Engel, Z. Phys. C 66 (1995) 203; R. Engel and J. Ranft, Phys. Rev. D 54 (1996) 4244.

[50] U. Bassler and G. Bernardi, Nucl. Instr. Meth. A 361 (1995) 197.

[51] CTEQ Collab., H.L. Lai et al., Phys. Rev. D 55 (1997) 1280.

[52] S. Catani, Int. Symposium on Lepton Photon Interactions, Hamburg, Germany (1997) and hep-ph/9712442.

[53] A.D. Martin, R.G. Roberts, W.J. Stirling and R.S. Thorne, Eur. Phys. J. C 4 (1998) 463.

[54] M. Glück, E. Reya and A. Vogt, Z. Phys. C 67 (1995) 433.

[55] F. James and M. Roos, Comp. Phys. Comm. 10 (1975) 343.

[56] F. Zomer, Proceedings of the workshop on deep-inelastic scattering and QCD (DIS97), eds. D. Krakauer and J. Repond, Chicago, Illinois (1997).

[57] G. Lobo, Proceedings of the workshop future physics at HERA, eds. G. Ingelman, A. De Roeck and R. Klanner, DESY, Hamburg (1996) 537.

[58] H1 Collab., contributed paper 260 to ICHEP 97, Jerusalem, Israel (1997).